Acta Pharmaceutica Sinica B 2024;14(11):4977–4993

Chinese Pharmaceutical Association
Institute of Materia Medica, Chinese Academy of Medical Sciences

Acta Pharmaceutica Sinica B

www.elsevier.com/locate/apsb
www.sciencedirect.com

ORIGINAL ARTICLE

Colon-specific controlled release of oral liposomes for enhanced chemo-immunotherapy against colorectal cancer

Mengya Niu[a,b], Yihan Pei[a,b], Tiantian Jin[a,b], Junxiu Li[a,b], Liming Bai[a,b], Cuixia Zheng[c], Qingling Song[a,b], Hongjuan Zhao[a,b,*], Yun Zhang[a,b,*], Lei Wang[a,b,*]

[a]*School of Pharmaceutical Sciences, Zhengzhou University, Zhengzhou 450001, China*
[b]*Henan Key Laboratory of Nanomedicine for Targeting Diagnosis and Treatment, Zhengzhou 450001, China*
[c]*Henan University, Huaihe Hospital, Translational Medicine Center, Kaifeng 475000, China*

Received 20 June 2024; received in revised form 8 August 2024; accepted 18 August 2024

KEY WORDS

Colorectal cancer;
Colon-specific delivery;
Oral liposomes;
Oxaliplatin;
Intratumoral bacteria;
Chemo-immunotherapy;
Clostridium butyricum spores;
Gut microbiota

Abstract A colon-specific drug delivery system has great potential for the oral administration of colorectal cancer. However, the uncontrollable *in vivo* fate of liposomes makes their effectiveness for colonic location, and intratumoral accumulation remains unsatisfactory. Here, an oral colon-specific drug delivery system (CBS-CS@Lipo/Oxp/MTZ) was constructed by covalently conjugating *Clostridium butyricum* spores (CBS) with drugs loaded chitosan (CS)-coated liposomes, where the model chemotherapy drug oxaliplatin (Oxp) and anti-anaerobic bacteria agent metronidazole (MTZ) were loaded. Following oral administration, CBS germinated into *Clostridium butyricum* (CB) and colonized in the colon. Combined with colonic specifically β-glucosidase responsive degrading of CS, dual colon-specific release of liposomes was achieved. And the accumulation of liposomes at the CRC site furtherly increased by 2.68-fold. Simultaneously, the released liposomes penetrated deep tumor tissue *via* the permeation enhancement effect of CS to kill localized intratumoral bacteria. Collaborating with blocking the translocation of intestinal pathogenic bacteria from lumen to tumor with the gut microbiota modulation of CB, the intratumoral pathogenic bacteria were eliminated fundamentally, blocking their recruitment to immunosuppressive cells. Furtherly, synchronized with lipopolysaccharide (LPS) released from MTZ-induced dead *Fusobacterium nucleatum* and the tumor-associated antigens produced by Oxp-caused immunogenic dead cells, they jointly enhanced tumor infiltration of $CD8^+$ T cells and reactivated robust antitumor immunity.

*Corresponding authors.
E-mail addresses: zhaohongjuan@zzu.edu.cn (Hongjuan Zhao), zhangyun@zzu.edu.cn (Yun Zhang), wanglei1@zzu.edu.cn (Lei Wang).
Peer review under the responsibility of Chinese Pharmaceutical Association and Institute of Materia Medica, Chinese Academy of Medical Sciences.

https://doi.org/10.1016/j.apsb.2024.09.015

1. Introduction

Oral administration is preferred for colorectal cancer (CRC) treatment due to its convenience and high patient compliance[1]. Nanocarriers have presented great potential for oral delivery of antitumor drugs[2]. Among these, liposomes stand out for their excellent encapsulation capacity, biocompatibility, and safety, making them a long-standing focus for drug carrier research. However, the uncontrollable fate of liposomes (payload leakage and limited drug availability at the tumor site) is the biggest obstacle limiting their oral application[3]. Therefore, enhancing the stability and controllable distribution of oral liposomes is of utmost importance in improving CRC efficacy.

Although modified liposomal surfaces with natural or synthetic polymer coatings have been demonstrated as effective elements to improve liposomal stability, there is still a challenge in effective drug delivery[4]. Colon is a favorable site for drug delivery of orthotopic CRC due to bypassing the first-pass metabolism, a longer residence time, decreased drug dose, and systemic side effects[5]. Nevertheless, due to the uncontrollable distribution of oral liposomes in the gastrointestinal tract (GIT), most oral liposomes are absorbed systemically from the small intestine, making it difficult to reach the colon segment. The effectiveness for colonic location and intratumoral accumulation of oral liposomes remains unsatisfactory.

Clostridium butylicum (CB), a strictly anaerobic probiotic with endospore-producing, has been widely used in treating digestive system diseases, including inflammatory bowel disease and gastrointestinal tumors[6–9]. Butyrate, a main product of CB, can not only sensitize chemotherapy treatment but also enhance the infiltration of $CD8^+$ T cells[10,11]. However, the harsh gastrointestinal environment leads to a low survival rate and colonization efficiency of oral probiotics. CB spores (CBS), a dormant form of CB, have natural resistance to harsh acidic and alkaline environments, toxic chemicals, extreme temperatures, and other factors[12,13]. More importantly, CBS shells rich in −COOH reactive groups are highly suitable for loading chitosan (CS) coated liposomes by forming covalent bonds with $-NH_2$ of CS[14]. In addition, after absorbing intestinal water and nutrients, CBS germinates specifically in the anaerobic colon, which is beneficial for precisely colonic-specific controlled release of oral liposomes by combining with colonic specifically β-glucosidase responsive degrading of CS.

Moreover, the low efficacy of oral chemotherapy is not only due to the unsatisfactory delivery efficiency mentioned above but also the presence of intratumoral pathogenic bacteria, especially in CRC. Research has shown that pathogenic bacteria translocate from the lumen to the tumor tissue because of microbiota dysbiosis and intestinal barrier dysfunction[15]. They induce chemotherapy tolerance of CRC by activating autophagy, inhibiting apoptosis, and impairing the immune microenvironment inhibition[16–20]. Recent studies have shed light on the unique advantages of probiotics in synergy with chemotherapy[21–23]. By physiochemical modification or genetic engineering of probiotics, Probiotic therapy can enhance the efficacy of chemotherapy and reduce side effects such as gastrointestinal reactions caused by drug leakage during the treatment process[22–24]. Interestingly, after germination, internal nutrient cells of CBS are generated and grow back into probiotics CB, which can reconstruct the intestinal microbiota and repair the damaged intestinal barriers by secreting short-chain fatty acids (SCFAs) and competing with pathogenic bacteria for colonization, blocking the supplementation pathway of intratumoral bacteria fundamentally. Metronidazole (MTZ), a frontline anti-anaerobic bacteria drug loaded into liposomes, can kill the localized intratumoral pathogenic bacteria[25,26]. MTZ-induced intratumoral bacteria death not only blocks the recruitment of immunosuppressive cells by pathogenic bacteria (such as *Fusobacterium nucleatum* and *Escherichia coli*) but also promotes dendritic cell (DC) maturation and macrophage polarization by releasing lipopolysaccharide (LPS) as immune adjuvants[27,28]. Together with immunogenic cell death (ICD) caused by oxaliplatin (Oxp), they promote $CD8^+$ T cell infiltration and reactivate antitumor immunity[29]. Unfortunately, MTZ is a broad-spectrum antibiotic that can directly lead to microbial dysbiosis when taken orally. Therefore, improving the stability and controllable distribution of oral liposomes is even more important.

Based on the above analysis, we constructed an orally microbial formulation (CBS-CS@Lipo/Oxp/MTZ) using a model chemotherapy drug Oxp, in combination with an antibiotic agent MTZ, both loaded into CS-coated liposomes and subsequently conjugated with CBS *via* covalent bonds (Scheme 1). By the synergism of the colon-specific germination of CBS and colon-specific enzyme-responsive degradation of CS, the intratumoral accumulation of oral liposomes was enhanced significantly. Furtherly, the antibiotic agent MTZ delivered into tumor tissue localized killed the intratumoral bacteria. Combined with blocking their supplementation pathway by regulating gut microbiota with CBS, the killing of intratumoral pathogenic bacteria was fundamentally achieved. Collaborating with SCFAs produced by CB, LPS released from MTZ-induced dead *F. nucleatum* and tumor-associated antigens released by Oxp-caused immunogenic dead cells jointly promoted the immune cytotoxicity of $CD8^+$ T cells and enhanced their tumor infiltration, reactivating robust the efficacy of chemo-immunotherapy.

2. Materials and methods

2.1. Chemicals and reagents

Oxaliplatin (Oxp, 99.0%), Metronidazole (MTZ, >99.0%), 1 ethyl 3-(3 dimethylaminopropyl carbodiimide (EDC, 98.0%) and *N*-hydroxysulfosuccinimide (NHS, 98.0%) were purchased from Aladdin Reagent Co., Ltd. (Shanghai, China). Chitosan (MWCO 5000 kDa) was purchased from Shanghai Macklin Biochemical Co., Ltd. (Shanghai, China). 1-α-Phosphatidylcholine (PC), cholesterol (Chol), and fluorescein isothiocyanate isomer I (FITC, 90%) was bought from Solarbio Co., Ltd. (Shanghai, China). Polyethylene glycol-conjugated 1,2-distearoyl-*sn*-glycero-3-phosphoethanolamine ($DSPE\text{-}PEG_{2000}$) was purchased from Shanghai Ponsure Biotechnology Co., Ltd. (Shanghai, China). The

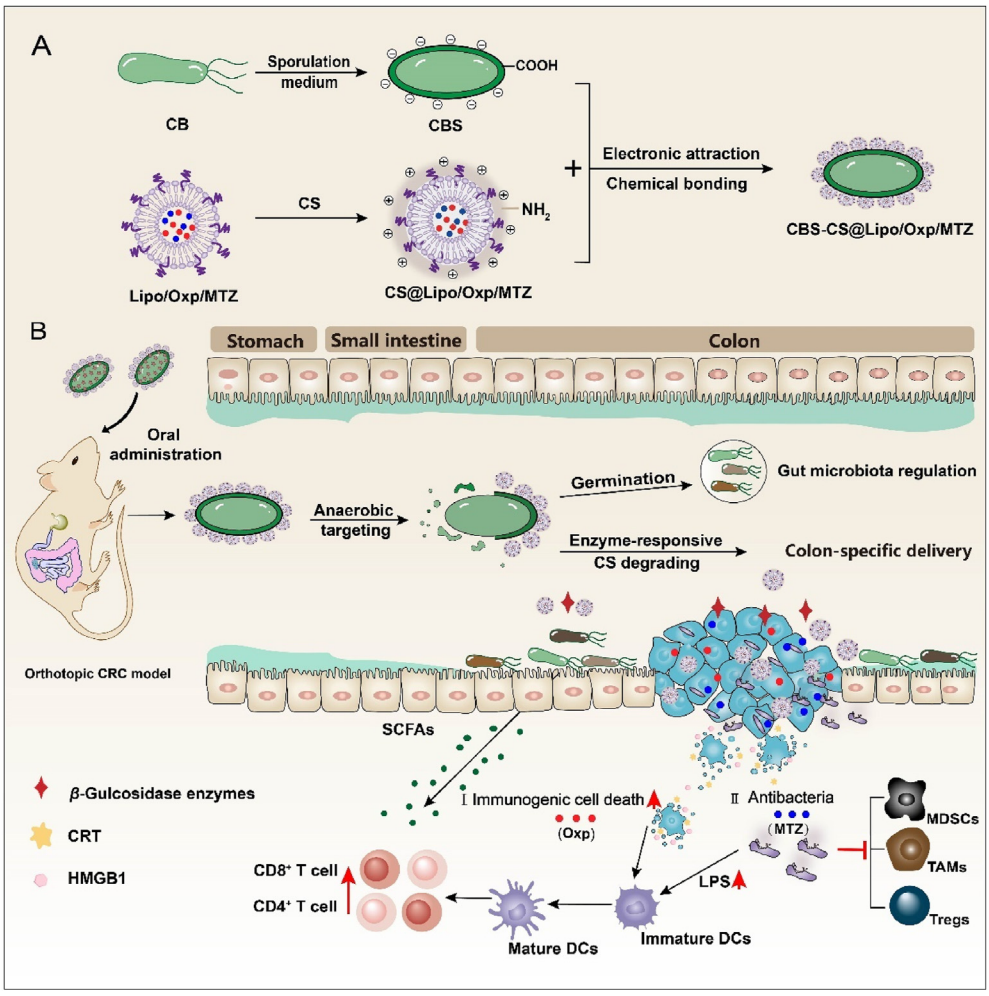

Scheme 1 Schematic illustration of the synthesis and mechanism of CBS-CS@Lipo/Oxp/MTZ for orthotopic colorectal cancer therapy.

surface marker antibodies for flow cytometry were purchased from Becton Dickinson Company (USA). The chemicals mentioned above were of analytical grade and used without any additional purification.

2.2. *Synthesis of CBS-CS@Lipo/Oxp/MTZ*

The thin-film hydration method was used to encapsulate hydrophilic drugs, as stated in the literature[30]. A certain molar ratio of lipid materials, including phospholipids, cholesterol, and DSPE-PEG_{2000}, was precisely weighed, and 2 mL of chloroform was added to dissolve the above materials to form an organic phase. Firstly, a 1.5 mL aqueous solution of MTZ and Oxp was taken as the aqueous phase and added dropwise to the organic phase under the condition of ultrasound in a water bath. The mixture was kept shaking while adding until a uniform W/O type emulsion was formed. After shaking, the emulsion did not hang on the wall and could drip down along the wall of an eggplant-shaped bottle. Secondly, the chloroform was completely removed using a rotary evaporator for 30 min. Then, 2 mL of water was added, and the mixture was incubated at 45 °C for 1 h to produce Lipo/Oxp/MTZ. Furtherly, 2 mg/mL CS in 1% acetic acid solution was added dropwise and stirred at room temperature for 1 h to obtain CS@Lipo/Oxp/MTZ after removing free CS through dialysis. After the carboxyl group of CBS was activated for 30 min with EDC and NHS, CS@Lipo/Oxp/MTZ was dropwise added and stirred for 40 min to obtain CBS-CS@Lipo/Oxp/MTZ.

2.3. *Characterization of CBS-CS@Lipo/Oxp/MTZ*

Multiple detection methods were utilized to investigate the construction of CS@Lipo/Oxp/MTZ attached to CBS. Confocal laser scanning microscopy (CLSM, Leica TCS SP8*, Germany), transmission electron microscopy (TEM, JEOL, Japan), Fourier transform infrared spectroscopy (FT-IR, Thermo, USA), nuclear magnetic resonance hydrogen spectrum (^{1}H NMR, AVANCE, Switzerland) and fluorescence-activated cell sorting (FACS) flow cytometry techniques were used. The size distribution and zeta potential were measured by a dynamic light scattering (DLS) analyzer (Zetaster, Malvern, UK). Drug loading and encapsulation rate were determined by inductively coupled plasma mass spectrometry (ICP-MS, PerkinElmer, England). The stability and physiological activity of CBS-CS@Lipo/Oxp/MTZ were evaluated in simulated gastric fluid (SGF) supplemented with pepsin, simulated intestinal fluid (SIF) containing trypsin, bile salts and simulated colonic fluid (SCF) with β-glucosidase at 37 °C, respectively and furtherly characterized by spread plate, CLSM, and TEM.

2.4. Drug loading of CBS-CS@Lipo/Oxp/MTZ

A 1.5 mL aqueous solution of MTZ (5 mg) and Oxp (5 mg) was taken to prepare CS@Lipo/Oxp/MTZ according to the thin-film hydration method. After the carboxyl group of CBS ($\sim 1 \times 10^9$ CFU) was activated for 30 min, CS@Lipo/Oxp/MTZ was dropwise added and stirred for 40 min to obtain CBS-CS@Lipo/Oxp/MTZ, which was freeze-dried and weighed. The content of the Pt element was detected by ICP-MS. The drug loading capacity efficiency of Oxp was calculated as Eq. (1):

$$\text{Drug loading efficiency (Oxp)} = \text{Oxp content/Total colonies of CBS (μg/CFUs)} \quad (1)$$

The powder was resuspended by PBS and the absorbance values of MTZ were detected by UV−Vis at wavelength of 320 nm. Then the absorbance value was substituted into the standard curve of MTZ to calculate the MTZ content. The drug loading capacity efficiency of MTZ was calculated as Eq. (2):

$$\text{Drug loading efficiency (MTZ)} = \text{MTZ content/Total colonies of CBS (μg/CFUs)} \quad (2)$$

2.5. Assessing the release behavior of CS@Lipo/Oxp/MTZ in GIT

To evaluate the release behavior of liposomes in GIT, 2 mL CBS-CS@Lipo/MTZ was incubated with SGF (pH 1.2), SIF (pH 6.8), and SCF (pH 7.4, with or without β-glucosidase, 5 U/mL, in an anaerobic gas bag) and placed at 37 °C. The operation times in different mediums were 2 h in SGF, 4 h in SIF, and the rest in SCF, corresponding to the food transport time of each GIT segment. 0.5 mL of the release medium was taken at specific time intervals, and 0.5 mL of the fresh release medium corresponding to the pH was supplemented. Samples at different time points were centrifuged at 4500 rpm for 5 min (Eppendorf, Germany). Then, the upper suspension was demulsified with Triton X-100. After centrifugation at 12,000 rpm for 10 min (Eppendorf), the absorbance of MTZ at 320 nm was determined by UV−Vis to quantify the content of MTZ at different time points. The release percentage of liposomes was calculated as Eq. (3):

$$\text{Released liposomes (\%)} = \text{MTZ content in upper suspension/MTZ content in CBS-CS@Lipo/MTZ} \times 100 \quad (3)$$

2.6. Bacteria and cell line culture

CB (CCTCC M2022151), Gram-positive anaerobe bacteria, was used and cultured in brain heart infusion (BHI) broth within a gas chamber using the anaerobic gas-producing bag at 37 °C. 4 mL of primary bacterial solution was inoculated into 100 mL growth medium and cultured in a 37 °C incubator for 24 h to obtain the second-generation bacterial solution. CBS was isolated with a sporulation medium by adding $CaCl_2$ (5 mg/mL) to the BHI medium. The model pathogenic bacteria utilized in this research was *F. nucleatum* (ATTCC 25586), a Gram-negative anaerobe that was grown in modified BHI broth at 37 °C in an anaerobic gas chamber. Colon cancer cell line CT26-luc was cultured in RPMI 1640 medium with 10% fetal bovine serum (FBS) and 1% penicillin/streptomycin at 37 °C with 5% CO_2.

2.7. In vitro antibiosis activity

To assess the antibiosis activity, we cocultured *F. nucleatum* with free MTZ or CS@Lipo/Oxp/MTZ for 24 h. Furtherly, the concentration range of MTZ was set from 1 to 10^{-8} mg/mL. Then, the above bacterial liquid was seeded in 96-well plates (200 μL/well) to measure the absorbance at 600 nm (OD_{600}) by a microplate reader (Bio-Rad, USA). The bacteria without MTZ treatment were used as controls.

2.8. Isolation of bone marrow-derived macrophages (BMDMs) and bone marrow-derived dendritic cells (BMDCs)

BMDMs were isolated as previously mentioned[31]. In more detail, the femurs and tibias of C57BL/6 mice were stripped of any muscle tissue using gauze before the bones were placed in a 60 mm dish with 75% alcohol for 1 min, washed twice with PBS, and then moved into a new dish with RPMI 1640. With a sterile syringe and 1 mL of PBS, the marrow was flushed out after the ends of the bones were severed with scissors in the dish. The acquired tissue was suspended, then the red blood cells were lysed using ACK lysis buffer while the tissue was run through a cell strainer (Falcon, 70 μm) to remove tiny fragments of bone and debris. Then, the BM cells were cultured at 2×10^6 cells per well in six-well plates in DMEM containing 10% (*v*/*v*) FBS and 1% penicillin/streptomycin for 6 days. Every three days, new media was introduced to cells being cultivated at 37 °C. Subsequently, LPS (100 ng/mL) and interferon-gamma (IFN-γ, 10 ng/mL) were added to the medium for 24 h to obtain M1 phenotype macrophages. Similarly, the bone marrow-derived cells were cultured at 1×10^6 cells per well in six-well plates with RPMI 1640 medium containing 20 ng/mL GM-CSF for 6 days. The surface markers CD80 and CD86 were used to identify BMDCs.

2.9. Stimulation of BMDMs and BMDCs with conditioned medium containing F. nucleatum supernatant

After coculturing *F. nucleatum* with CBS-CS@Lipo/Oxp/MTZ anaerobically for 12 h, the supernatant was collected by centrifugation at 8000 rpm/min (Eppendorf). The bacterial nucleic acid was removed by adding nuclease. Then the resulting supernatant was boiled at 100 °C for 10 min to inactivate any residual protein and was further filtered using an injection filter (0.2 μm) to remove bacteria that retain intact biofilms. Subsequently, the bacterial supernatant obtained above was diluted with fresh DMEM or RPMI 1640 (1:20) to form a conditioned medium containing *F. nucleatum* supernatant. Then, M1-like phenotype BMDMs or BMDCs were incubated with the above supernatant for 24 h. Commercially available LPS (10 μg/mL) was used as a positive control, and the percentage of $F4/80^+CD86^+$ M1-like phenotype macrophages and $CD80^+CD86^+$ BMDCs were detected by flow cytometry.

2.10. Transwell migration assay

CT26 cells were cocultured with *F. nucleatum* (multiplicity of infection (MOI) 100:1) for 6 h and then were treated with CS@Lipo/Oxp/MTZ for 24 h. The migration assay was carried out as previously described[32]. The migrated cells in the basolateral

side of the upper chamber were stained with crystal violet and photographed for recording.

2.11. Bacteria/tumor spheroids coculture assay

Firstly, the 3D tumor spheroids were constructed as the literatures[33,34]. Cells were reselected in fresh culture medium without antibiotics and then added to a 96-well ultra-low attachment spheroid microplate at a volume of 200 μL per well. The semi-quantitative fluid exchange was performed every other day, and after 5−7 days of cultivation, 3D tumor spheroids could be formed. Subsequently, *F. nucleatum* (OD_{600} = 0.1) was added to the culture medium for coincubation for 24 h. The old culture medium was discarded, and a fresh culture medium was added to obtain the bacterial/tumor spheroids coculture system.

2.12. Cytotoxicity assay

To evaluate the effect of *F. nucleatum* on the cytotoxicity of various formulations, we seeded CT26 cells in 96-well plates with a density of 8000 cells per well. Respectively, the cells were cocultured with PBS, Oxp, CS@Lipo/Oxp, CS@Lipo/Oxp/MTZ for 24 h after co-incubation with *F. nucleatum* for 6 h. Then the CCK-8 was used to detect the cell viability of the groups with different treatments.

2.13. Cellular uptake and lysosomal escape

CT26 cells were plated in 6-well plates (3×10^5 cells/well) and incubated for 24 h. The free FITC and CS@Lipo/FITC (4 μg/mL) were incubated for 1, 2 and 4 h, respectively. Then the lysosomes were labeled with Lyso-Tracker Red (50 nmol/L) and the nucleus was stained with Hochst 33342 dye (10 μg/mL). Finally, CLSM and flow cytometry were employed to evaluate phagocytic uptake and lysosomal escape.

2.14. Annexin V-FITC/PI assay and Calcein-AM/PI double stain

There are four experimental groups including Control, CS@Lipo, CS@Lipo/Oxp and CS@Lipo/Oxp/MTZ. The Annexin V-FITC/PI cell apoptosis kit was used to analyze cell apoptosis according to the instructions. For the Live/Dead assay, after co-incubating the above formulations with cells for 24 h, the Calcein-AM/PI working solution was added and incubated for 20 min. A fluorescence microscope was employed to capture images.

2.15. Establishment of orthotopic CRC animal model

As described in the literature[33], a model of orthotopic colon cancer was established by repeatedly scraping the area of abundant blood supply in the cecum and then sticking CT26-luc solid tumor to the scraping area with biological tissue adhesive. Subsequently, d-fluorescein (150 mg/kg) was injected intraperitoneally at different time points, and the abdominal bioluminescence intensity was observed using an IVIS imaging system (PerkinElmer, USA).

2.16. Biodistribution of CBS-CS@Lipo/IR783

To evaluate the accumulation of nanoliposomes at the tumor site, we treated mice with free IR783, CS@Lipo/IR783, and CBS-CS@Lipo/IR783 (1 mg/kg). The biodistribution of IR783 was observed by an IVIS Imaging System (Bruker, Germany) at specific points (Ex = 630 nm, Em = 780 nm). After that, all groups of mice were euthanized, and the gastrointestinal tract, heart, liver, spleen, lung, kidney, and tumor tissues were removed for fluorescence imaging, and the fluorescence intensity of each tissue was further quantified by the living imaging software.

2.17. Pharmacokinetic study

Rats were given oral doses of free Oxp, CS@Lipo/Oxp/MTZ, and CBS-CS@Lipo/Oxp/MTZ (Oxp: 10 mg/kg). Plasma was separated from blood samples by centrifuging them at 3500 rpm for 15 min (Eppendorf) after they were drawn from the retro-orbital plexus at predetermined time intervals (5, 10, 15, 30, 45 min, and 1, 2, 4, 8, 10, 12, 24 h). Then the supernatant of the main organs was obtained by homogenizing and centrifuging at 12,000 rpm for 15 min (Eppendorf). Finally, the blood and tissue concentration of platinum (Pt) was quantitatively examined by ICP-MS.

2.18. Antitumor efficacy evaluation in vivo

Balb/c mice bearing orthotopic CRC were employed to evaluate the *in vivo* antitumor efficacy of the CBS-CS@Lipo/Oxp/MTZ. Tumor-bearing mice were divided into seven groups including PBS (−), PBS (+), CBS (+), CS@Lipo (+), CS@Lipo/Oxp (+), CS@Lipo/Oxp/MTZ (+), CBS-CS@Lipo/Oxp/MTZ (+) (wherein (+) and (−) were referred with or without *F. nucleatum* infection). The groups with *F. nucleatum* infection were orally administrated *F. nucleatum* 3 times for one week (100 μL, 1×10^8 CFU/mL). The mice were treated with different formulations at a concentration of 10 mg/kg (CBS, 2×10^8 CFU/day, 200 μL) every other day After two weeks of administration, tumor-bearing mice were intraperitoneally injected with d-fluorescein (150 mg/kg) every 4 days. Then, the mice were anesthetized and photographed under the IVIS Imaging System to monitor tumor growth changes. After the administration, the mice in each group were euthanized. The tumor size was photographed, and the tumor weight was recorded after the tumors were dissected. To test the antibacterial effect of the formulations against intratumoral bacteria, the tumor tissue was then homogenized by a tissue grinder, and the supernatant was utilized for the spread plate. Ensure that each step is carried out under sterile conditions. For characterizing the histopathological changes, tumor tissues were stained by hematoxylin and eosin (H&E) staining, terminal deoxynucleotidyl transferase-mediated dUTP-biotin nick end labeling (TUNEL), Ki67, and ICD markers: calreticulin (CRT) and high mobility group proteins B1 (HMGB1). Tumor of liver metastasis was characterized by H&E staining.

2.19. Detection of tumor-infiltrating lymphocytes

To detect the immune status of tumor tissues after administration, the tumor tissues were digested into single-cell suspensions. The immune cells isolated from mice were stained with the following surface marker antibodies: APC-Cyanine7-conjugated anti-CD45, FITC-conjugated anti-CD11b, BV421-conjugated anti-CD11c, PE/Cyanine7-conjugated anti-Gr-1, AF647-conjugated anti-F4/80, PE-conjugated anti-CD206, PerCP-conjugated anti-CD86, PE-conjugated anti-CD80, BV510-conjugated anti-CD3, PE/Cyanine7-conjugated anti-CD4, AF700-conjugated anti-CD8, APC-conjugated anti-Foxp3. Flow cytometry was conducted by

FACSCanto II (BD Biosciences, Franklin, NJ, USA) and data was analyzed using FlowJo software (Ashland, OR). ELISA assay was used to detect the serum cytokines, including tumor necrosis factor-α (TNF-α) and IFN-γ.

2.20. *Modulation on gut microbiota*

To evaluate the potential effect of CBS-CS@Lipo/Oxp/MTZ on intestinal microbiota modulation, we collected fecal samples for 16S rDNA gene sequencing after administration (Meiji Co., Ltd., Shanghai, China). The samples of successfully constructed libraries were analyzed to illustrate the impact of different treatments on the gut microbiota.

2.21. *Biosafety assessment*

After the administration, blood was collected for hematological parameters and biochemical indicators testing. For the main tissues (heart, liver, spleen, lung, kidney) of experimental mice, H&E staining was carried out to perform pathological analysis.

2.22. *Study approval*

All experimental procedures were executed according to the protocols approved by Zhengzhou University Animal Care and Use Committee (yxyllsc20240043).

2.23. *Statistical analysis*

The data were presented as the mean ± standard deviation (SD). The level of significance was indicated at probabilities: $*P < 0.05$, $**P < 0.01$, $***P < 0.001$, n.s, no significance.

3. Results and discussion

3.1. *Preparation and characterization of CBS-CS@Lipo/Oxp/MTZ*

The Lipo/Oxp/MTZ was synthesized using a thin-film hydration method[30]. Subsequently, 2 mg/mL CS in 1% acetic acid solution was added into Lipo/Oxp/MTZ dropwise and stirred at room temperature for 1 h. Owing to the strong electrostatic interaction between positively charged CS and negatively charged Lipo/Oxp/MTZ, CS@Lipo/Oxp/MTZ was obtained steadily. The morphology of Lipo/Oxp/MTZ and CS@ Lipo/Oxp/MTZ was detected by TEM (Fig. 1A and B). Subsequently, CBS was decorated with CS@Lipo/Oxp/MTZ by electrostatic interaction and amido bonds. The chemical structures of CBS, CS@Lipo, and CBS-CS@Lipo were characterized by FT-IR and ^{1}H NMR, respectively. For the FT-IR of CBS, the strengthened stretching vibration peak at 1644 cm^{-1} of C=O was observed; 1621 cm^{-1} was the stretching vibration peak of the N−H bond on CS, and CBS@CS/Lipo exhibited stretching vibration peaks of amide I and amide II bands at 1636 and 1565 cm^{-1}, indicating that CS@Lipo/Oxp/MTZ was successfully conjugated to CBS (Fig. 1C). Ulteriorly, ^{1}H NMR spectrum of CBS-CS@Lipo retained the characteristic peaks of both CBS and CS@Lipo and the generation of new chemical shifts indirectly indicated the formation of new chemical bonds, which furtherly demonstrated that CBS-CS@Lipo was successfully prepared (Supporting Information Fig. S1). Then, the representative TEM and SEM images showed that there were nanoliposomes-like substances on the surface of CBS (Fig. 1D−G). The element mapping results in Fig. 1H showed the presence of Pt element, which further verified the successful conjugation of CBS-CS@Lipo/Oxp/MTZ.

Moreover, the images by CLSM showed that FITC-labeled CS@Lipo colocalized with CBS, while the bare CBS possessed no or minimal background, which revealed that CS@Lipo was attached to the surface of CBS successfully (Fig. 1I). These results were also confirmed with the intensity distribution histograms of CBS-CS@Lipo/FITC (Fig. 1J). The fluorescence intensity distributions of CBS-CS@Lipo/FITC extend to higher intensities than those observed for bare CBS, and the FITC$^+$ percentage was changed from 6.16% ± 0.68% (CBS) to 81.8% ± 3.96% (CBS-CS@Lipo/FITC) (Supporting Information Fig. S2). In the process of CBS-CS@Lipo/Oxp/MTZ construction, the size was changed from 139.5 ± 15.4 (CS@Lipo/Oxp/MTZ) to 1872 ± 133 nm (CBS-CS@Lipo/Oxp/MTZ) (Fig. 1K). The zeta potential was changed from +35.2 ± 2.4 mV to +12.7 ± 1.8 mV (Fig. 1L). Moreover, the entrapment efficiency and drug loading efficiency of Oxp were 26.4% and 0.66 μg/10^6 CFUs measured by ICP-MS, and those of MTZ were 29.7% and 0.75 μg/10^6 CFUs measured by UV−Vis according to Eqs. (1) and (2).

3.2. *The stability of CBS-CS@Lipo/Oxp/MTZ in vitro*

Accumulating evidence shows that probiotic spores can resist ultraviolet radiation, high temperatures, and harsh acidic environments due to their hydrophobic protein shell on the surface[34,35]. In this sense, probiotic spores can serve as an advantageous bioactive carrier for the oral drug delivery system. Maintaining germination activity after surface modification of CBS as an oral delivery carrier is the primary prerequisite for exerting antitumor activity. As shown in Fig. 2A and B, there was no significant difference in the number of colonies and OD_{600} in the CBS-CS@Lipo/Oxp, CBS-CS@Lipo/MTZ and CBS-CS@Lipo/Oxp/MTZ groups compared to CBS group, and the colony morphology of all groups on the plate was uniformly circular with a smooth and slightly raised surface, suggesting that surface modification on CBS did not affect the germination of CBS.

Then, to investigate whether the oral drug delivery system could resist the damage of gastric acid and enzymes, we observed the morphological changes of CBS and CBS-CS@Lipo under the SGF and SIF. As illustrated in Fig. 2C, CBS itself did not germinate and there was still a layer of nanoparticle-like substance on the surface of the modified CBS after 2 h in SGF. After further incubation in SIF for 4 h, the vegetative bodies inside the spores regrew into CB and the surface-modified nanoparticles also dropped off. Further imaging by CLSM showed that FITC-labeled CS@Lipo was colocalized with CBS in SGF, while FITC was mostly separated from the bacterial in SIF, but there were still some bacteria colocalized with FITC, which might be due to electrostatic interaction (Fig. 2D). Subsequently, we evaluated the stability of nanoliposomes by testing the cumulative release percentage of MTZ in SGF SIF and SCF according to Eq. (3). As displayed in Fig. 2E, there was a profound effect on the stability and controllable release of oral liposomes. In particular, the release of MTZ was less than 20% in the CBS-CS@Lipo/Oxp/MTZ group in SGF and the release percentage of CS@Lipo/Oxp/MTZ was only about 30% even after 6 h in SIF, indicating that most of the liposomes were transported to the colon effectively. The amount of drug release at pH 7.4 without β-glycosidase

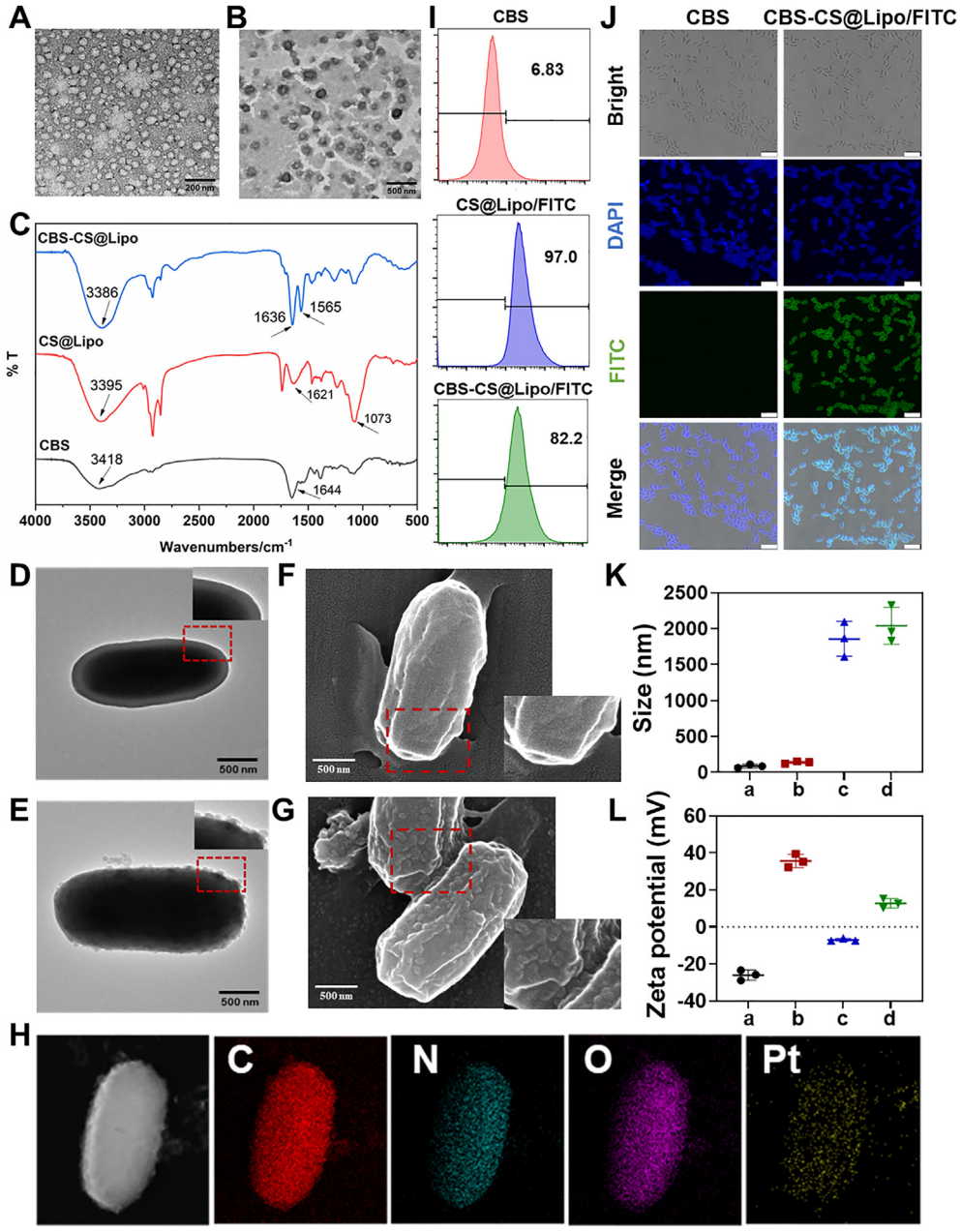

Figure 1 Preparation and characterization of CBS-CS@Lipo/Oxp/MTZ. Representative TEM images of (A) Lipo/Oxp/MTZ and (B) CS@Lipo/Oxp/MTZ. (C) FT−IR spectra of CBS, CS@Lipo, and CBS-CS@Lipo. Representative TEM images of (D) CBS and (E) CBS-CS@Lipo/Oxp/MTZ. Representative SEM images of (F) CBS and (G) CBS-CS@Lipo/Oxp/MTZ. (H) Element mapping analysis of CBS-CS@Lipo/Oxp/MTZ. (I) Flow cytometry histograms of CBS, CS@Lipo/FITC, and CBS-CS@Lipo/FITC ($n = 3$). (J) CLSM images of CBS and CBS-CS@Lipo/FITC. Scale bars: 5 μm. (K) Size and (L) Zeta potential of (a) Lipo/Oxp/MTZ, (b) CS@Lipo/Oxp/MTZ (c) CBS, and (d) CS@Lipo/Oxp/MTZ ($n = 3$).

was detected to be about 65.23%, indicating that the germination of CBS in an anaerobic colon environment is beneficial for precisely controlled colonic release of oral liposomes. In contrast, the amount of drug release at pH 7.4 with β-glycosidase was more than 80%, being attributed to the presence of CS that was degraded by the colon-specific enzyme β-glycosidase, thereby exhibiting superior enzyme-response properties. The above results indicated that CS@Lipo/Oxp/MTZ conjugated with CBS was beneficial for improving the colonic location and accumulation of oral liposomes.

3.3. *In vitro antibacterial activity*

To investigate the antibacterial activity of CS@Lipo/Oxp/MTZ, *F. nucleatum* was cultured in a modified BHI medium with or without CS@Lipo/Oxp/MTZ for 24 h. According to the OD600 of *F. nucleatum* treated with free MTZ in Supporting Information Fig. S3, when the MTZ concentration was as low as 1×10^{-8} mg/mL, it had a significant killing effect on Fn. Especially, when the concentration of MTZ was increased to 0.01 mg/mL, the growth of Fn would be completely suppressed, while the growth of

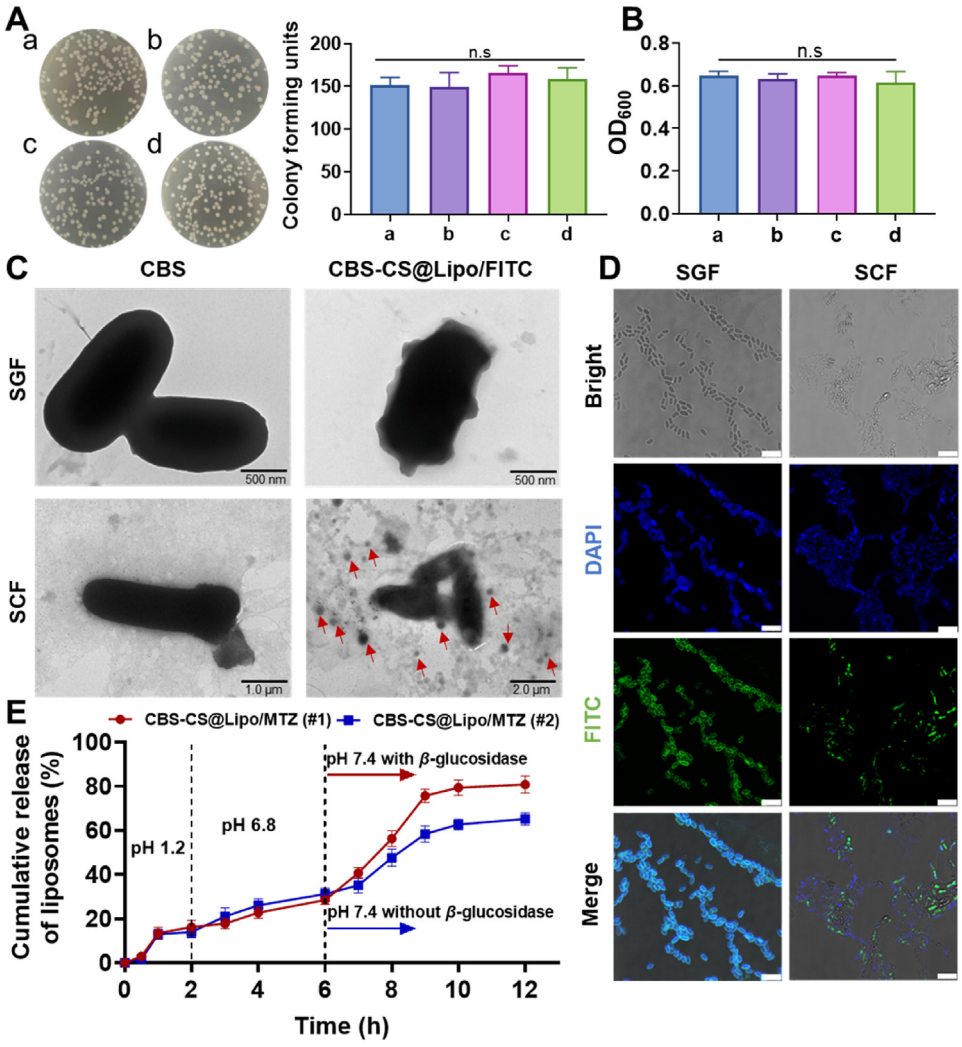

Figure 2 Characterization of modified CBS. (A) The spread plate and (B) OD_{600} of a) CBS, b) CBS-CS@Lipo/Oxp, c) CBS-CS@Lipo/MTZ, and d) CBS-CS@Lipo/Oxp/MTZ ($n = 3$). (C) TEM images of CBS and CBS-CS@Lipo/Oxp/MTZ after being incubated in SGF and SCF. (D) CLSM images of CBS-CS@Lipo/Oxp/MTZ after being incubated in SGF and SIF. Scale bar: 5 μm. (E) *In vitro* drug release profiles of CBS-CS@Lipo/Oxp/MTZ in SGF, SIF, and SCF ($n = 3$). Statistical analysis by one-way analysis of variance (ANOVA): $^{*}P < 0.05$; $^{**}P < 0.01$; $^{***}P < 0.001$, n.s, no significance.

CB was negligible suppressed. As shown in Fig. 3A, there was a significant decrease in OD_{600} of *F. nucleatum* from 1.96 to 0.28. The spread plate method was further employed to track the distribution of bacterial colonies. The bacteria of the control group fully covered the agar plates, while only sporadic colonies of the CS@Lipo/Oxp/MTZ group as seen in Fig. 3B. The TEM in Fig. 3C further showed that *F. nucleatum* in the control group remained intact and smooth, while severe destruction of the extracellular membrane was observed in CS@Lipo/Oxp/MTZ group. All the above results demonstrated the high antibacterial activity of CS@Lipo/Oxp/MTZ.

Furtherly, according to the literature, most of the bacteria present in tumor tissue were intracellular bacteria that evade recognition and clearance by immune cells and further promote tumor cell proliferation and migration[36,37]. The results in Fig. 3D−F showed that *F. nucleatum* could invade and penetrate the cancer cell membrane and colonize the tumor cells, while the fluorescence belonging to *F. nucleatum* disappeared after the treatment of CS@Lipo/Oxp/MTZ, which was further verified by the results of spread plate and TEM. Moreover, compared with the *F. nucleatum* group, the migrated cells after incubation with CS@Lipo/Oxp/MTZ were significantly decreased, which indicated that *F. nucleatum* could promote cell migration[38] (Fig. 3G).

Exogenous LPS, as an inducer of M1 polarization and DCs maturation, can induce an effective antitumor immune response[39−41]. To investigate whether the LPS released by damaged *F. nucleatum* after CS@Lipo/Oxp/MTZ treatment could activate an immune response. Conditioned medium containing *F. nucleatum*-released LPS was first prepared according to the method and co-incubated with BMDMs and BMDCs for 24 h. Commercial LPS was used as a positive control. As shown in Fig. 3H, the percentage of $F4/80^{+}CD86^{+}$ cells in the CS@Lipo/Oxp/MTZ group was 22.50%, ~4.0 fold higher than that in the control group (5.65%), indicating that LPS released by *F. nucleatum* could significantly promote macrophage polarization towards M1 phenotype. Similarly, the percentage of $CD80^{+}CD86^{+}$ BMDCs significantly increased from 5.37% to 22.10% in Fig. 3I.

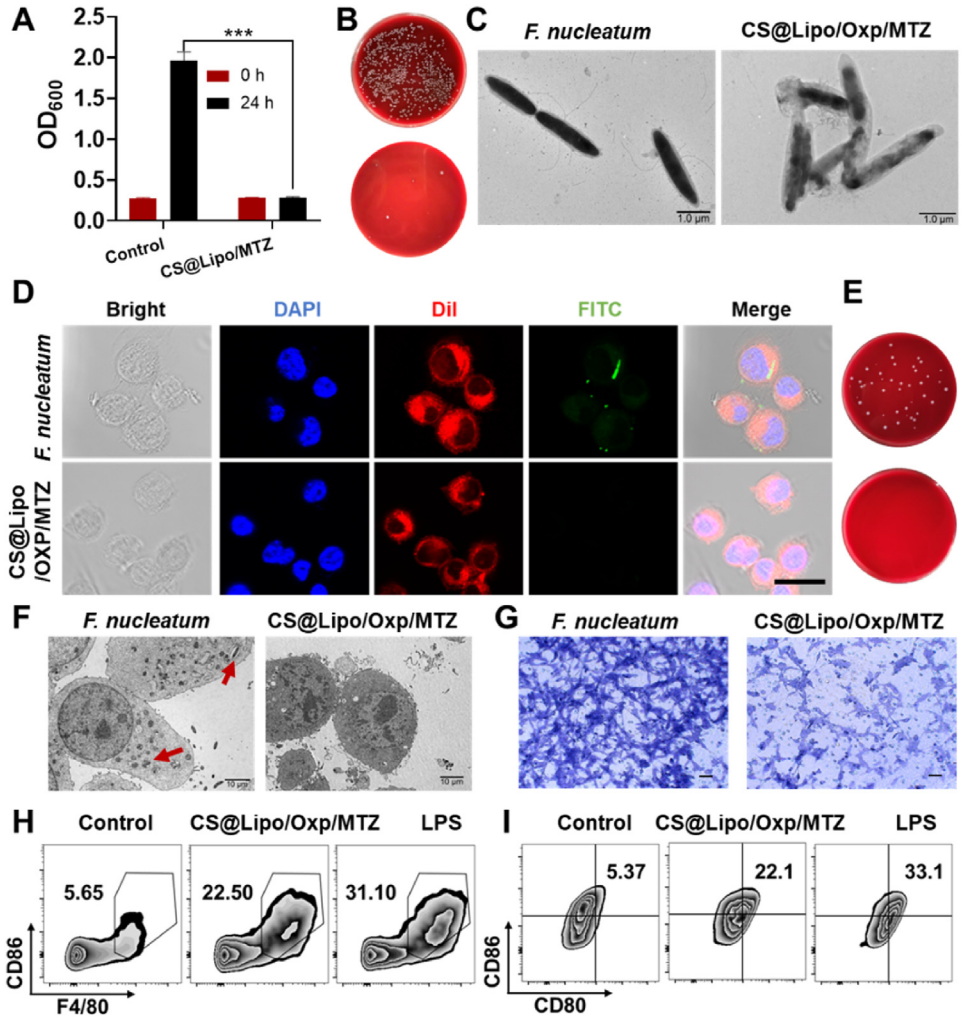

Figure 3 *In vitro* antibacterial activity. (A) OD_{600}, (B) Spread plate, and (C) TEM images of *F. nucleatum* treated with or without CS@Lipo/Oxp/MTZ ($n = 3$). (D) Fluorescence images of CT26 incubated with *F. nucleatum* for 6 h with or without CS@Lipo/Oxp/MTZ. Scale bar: 10 μm. (E) Spread plate of cell lysis after incubation with *F. nucleatum* for 6 h. (F) Representative TEM images of CT26 and (G) Migrated cells after incubation with *F. nucleatum* with or without CS@Lipo/Oxp/MTZ ($n = 3$). Scale bar: 100 μm. (H) Representative flow cytometric analysis of $F4/80^{+}CD86^{+}$ M1-like phenotype macrophages and (I) $CD80^{+}$ $CD86^{+}$ BMDCs after treatment with the conditioned media containing supernatants of *F. nucleatum*, and commercial LPS (10 μg/mL) was used as a positive control ($n = 3$). Statistical analysis by one-way analysis of variance (ANOVA): $^{*}P < 0.05$; $^{**}P < 0.01$; $^{***}P < 0.001$.

The flow cytometry results suggest that LPS released from *F. nucleatum* could elicit effective antitumor immunity.

3.4. *The enhanced antitumor activity of CBS-CS@Lipo/Oxp/MTZ in vitro*

Ideally, after arrival at the targeted tumor sites, CS@Lipo/Oxp/MTZ was released along with the germination of CBS and partly degradation of CS by β-glucosidase enzyme from colonic microflora. Then the released drugs could penetrate deep tumor tissues *via* the permeation enhancement effect of CS to eliminate intratumor *F. nucleatum* and induce ICD[42–45]. Hereby, we first evaluated the *in vitro* antitumor efficacy of CS@Lipo/Oxp/MTZ. It can be seen from Fig. 4A that Lipo/FITC could only penetrate to the position at a depth of 20 μm of the tumor spheroid, while CS@Lipo/FITC at 100 μm and distributed well inside the tumor spheroid, indicating that CS could significantly improve the permeability of nanoliposomes in the tumor spheroid. As depicted in Fig. 4B, after incubation with CT26 cells for 24 h, the cell cytotoxicity of CS@Lipo/Oxp/MTZ was detected by CCK-8. Consistent with the above figure, the cytotoxicity of Oxp was decreased significantly under the presence of *F. nucleatum*. Furtherly, there was a marked reduction in the cell viability of the CS@Lipo/Oxp/MTZ (+) group (42.3 ± 2.9%) compared with the Oxp (+) (64.3 ± 2.8%) group, suggesting the addition of MTZ could effectively inhibit chemotherapy resistance induced by *F. nucleatum*.

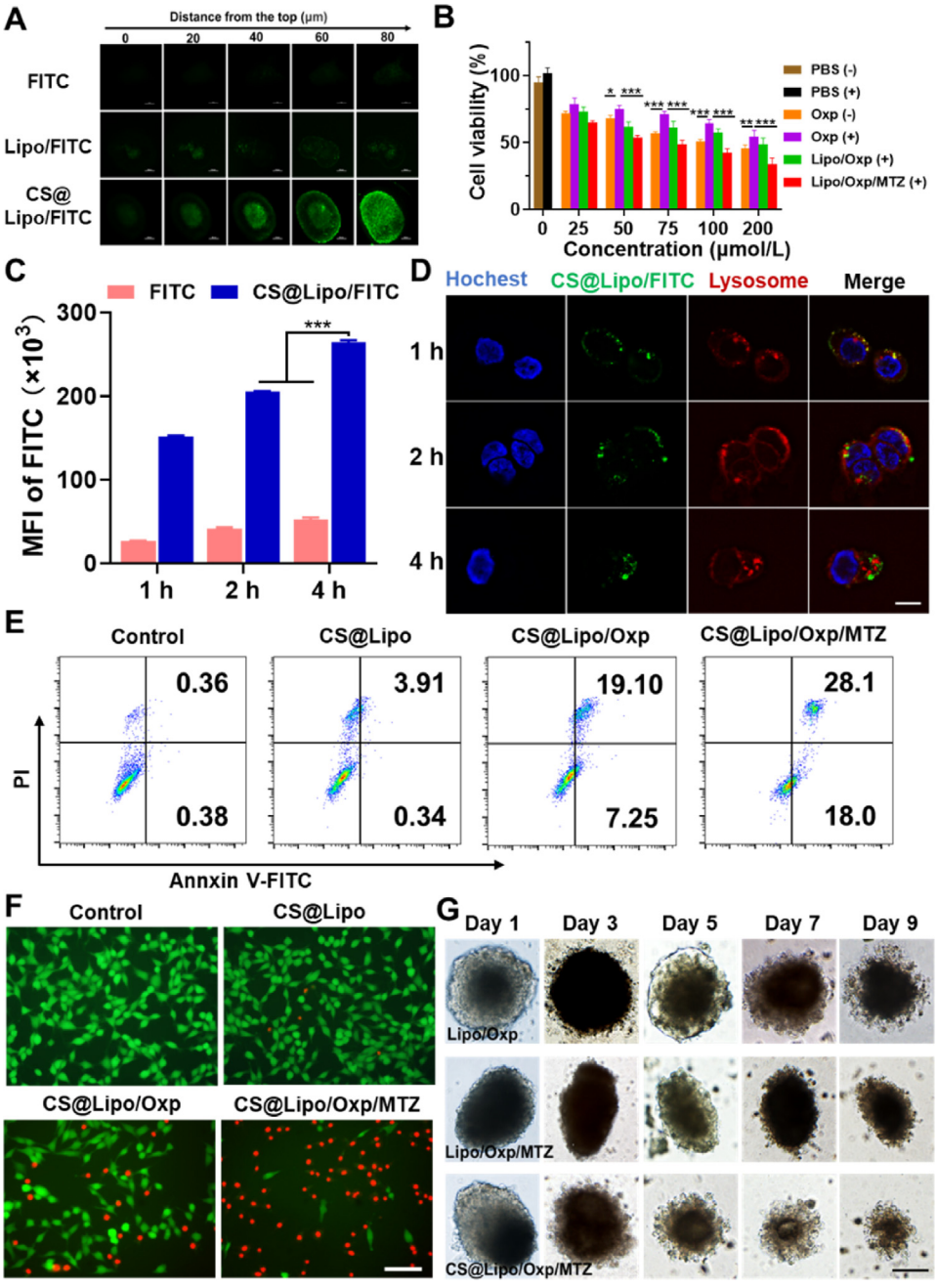

Figure 4 Tumor cytotoxicity of CS@Lipo/Oxp/MTZ under the presence of *F. nucleatum in vitro*. (A) The tissue penetration ability of FITC, Lipo/FITC, and CS@Lipo/FITC in 3D tumor spheroids. Scale bar: 100 μm. (B) Cell viability of CT26 treated with different formulations ($n = 3$). (C) The MFI of cellular uptake after treatment with FITC and CS@Lipo/FITC ($n = 3$). (D) Lysosomal escape of CS@Lipo/FITC. Scale bar: 10 μm. (E) Cell apoptosis experiment by flow cytometry ($n = 3$). (F) Images of CT26 cells stained with Calcein-AM and PI. Scale bar: 100 μm ($n = 3$). (G) The size of 3D tumor spheroids at different time points after treatment with Lipo/Oxp, Lipo/Oxp/MTZ, and CS@Lipo/Oxp/MTZ. Scale bar: 250 μm. Statistical analysis by one-way analysis of variance (ANOVA): $^*P < 0.05$; $^{**}P < 0.01$; $^{***}P < 0.001$.

Then CS@Lipo/FITC was employed to detect the cellular uptake through flow cytometry. The uptake percentage of FITC in CS@Lipo/FITC group reached 73.9% at 1 h and 83.1% at 4 h, significantly higher than that in the free FITC group (8.5% at 1 h and 18.4% at 4 h), being accompanied by a gradually increase in mean fluorescence intensity (MFI) over time (Fig. 4C). Furtherly, intracellular behavior of CS@Lipo/Oxp/MTZ liposomes was tracked by lysotracker. After incubation with CT26 for 1 h, most of the nanoparticles were colocalized with the red fluorescence of lysosomes. Part of the green fluorescence separated from red fluorescence at 2 h and most of the green fluorescence separated with the red fluorescence at 4 h (Fig. 4D). This might be due to the

amino protonation of chitosan consuming H^+ in the lysosomes and the increase of osmotic pressure leading to the rupture of the lysosome membrane and the subsequent release of payloads.

Next, we detected the apoptosis of CT26 cells after nanoparticles treatment using flow cytometry. As shown in Fig. 4E, the percentage of apoptotic and necrotic cells in the CS@Lipo/Oxp/MTZ group reached 46.1%, significantly higher than that in CS@Lipo/Oxp group (26.35%) and CS@Lipo group (4.25%). To characterize the living and dead cells more intuitively, we stained CT26 cells using the Calcein/PI double staining kit after different treatments and recorded them with a fluorescence microscope. The results were presented in Fig. 4F. Compared to other groups, the red fluorescence significantly increased, and the green fluorescence sharply decreased in the CS@Lipo/Oxp/MTZ group, indicating the excellent antitumor properties of the formulations.

To investigate the inhibitory effect of the formulations on the growth of 3D tumor spheroids in the presence of *F. nucleatum*, Lipo/Oxp, Lipo/Oxp/MTZ, and CS@Lipo/Oxp/MTZ were co-incubated with 3D tumor spheroids for 24 h, and observed under a microscope on days 1, 3, 5, 7, and 9. As shown in Fig. 4G, Lipo/Oxp and Lipo/Oxp/MTZ both showed a certain reduction in tumorsphere volume, while CS@Lipo/Oxp/MTZ group continued to decrease over time, indicating that the penetration effect of CS and the antibacterial effect of MTZ could significantly improve the antitumor efficacy of Oxp.

3.5. *The drug distribution in vivo*

Encouraged by the excellent antitumor effect *in vitro*, we further monitored the real-time fluorescence distribution of the IR783 labeled formulations *in vivo*. As shown in Fig. 5A, the abdominal fluorescence intensity of the free IR783 group mice peaked at 8 h, then gradually weakened, and almost completely disappeared at 96 h. The mice of the CS@Lipo/IR783 group and the CBS-CS@Lipo/IR783 group peaked at 24 h and there was still strong fluorescence in the left abdomen at 96 h. After 96 h, different groups of mice were euthanized and the fluorescence intensity of the main organs and tissues was detected using a small animal living imaging device. As shown in Fig. 5B and C, Supporting Information Fig. S4, the fluorescence in the intestine of CBS-CS@Lipo/IR783 and CS@Lipo/IR783 group mice was mainly concentrated at the tumor sites. There was a significant difference between the two groups ($P = 0.0122$). In addition, the fluorescence intensity of the tumor site of the CBS-CS@Lipo/IR783 group was significantly higher than that in other tissues. Encouraged by the above results, we carried out the pharmacokinetic experiments. Notably, although the plasma concentration of the CBS-CS@Lipo/Oxp/MTZ group was lower than that in the CS@Lipo/Oxp/MTZ group, the accumulation at the tumor site was significantly increased (Fig. 5D and E, Supporting Information Table S1), suggesting that after oral administration, part of the delivery system was absorbed into the blood circulation by the intestine, while the majority entered the colon segment under the targeting effect of CBS and colon specific enzyme-responsive degradation of CS.

3.6. *Anticancer efficacy of CBS-CS@Lipo/Oxp/MTZ in mice with orthotopic CRC*

The experiments of orthotopic CRC were established by following the timeline depicted in Fig. 6A. As displayed in Supporting Information Figs. S5A and S5B, the tumor had intertwined and grown tightly with the intestines and the tumor mass was shown after separation. Tumor-bearing mice were orally administered with formulations every other day for two weeks to evaluate the antitumor efficacy, and the body weight of mice was recorded simultaneously. As shown in Fig. 6B, there was a slight decrease in the body weight of mice during the administration, which suggest that loading Oxp in CS@Lipo could effectively reduce the toxicity of chemotherapy drug, although studies have shown that chemotherapy can lead to weight loss[46,47]. The tumor-bearing mice were subsequently monitored using bioluminescence imaging. The representative bioluminescence images in Fig. 6C showed that compared with PBS (−) group, the bioluminescence intensity of the PBS (+) group was significantly increased and no significant difference with the CS@Lipo group, indicating that *F. nucleatum* could promote tumor proliferation[48]. However, the CBS (+) group failed to slow the tumor proliferation, indicating that single probiotic therapy cannot effectively achieve an antitumor effect. While the bioluminescence intensity of the CBS-CS@Lipo/Oxp/MTZ group was significantly lower than that of the CS@Lipo/Oxp group. Consistently, as shown in Fig. 6D and Fig. S5C, the tumor tissues of the CBS-CS@Lipo/Oxp/MTZ group had the smallest volume and lightest weight after two weeks of treatment, which suggest the combination of probiotics with chemotherapy could significantly improve antitumor effect. Subsequently, the tumor tissue was then homogenized by a tissue grinder in a sterile environment, and the supernatant was utilized for the spread plate to test the antibacterial effect of the formulations against intratumor bacteria. As displayed in Fig. 6E, there was no antibacterial effect of the CS@Lipo/Oxp group compared with the PBS group. While the colony counts of CS@Lipo/Oxp/MTZ and CBS-CS@Lipo/Oxp/MTZ groups significantly decreased, which indicated that MTZ, a frontline antibiotic against anaerobic bacteria, has a significant antibacterial effect on *F. nucleatum*. However, there was still a significant difference in the number of bacterial colonies between the two groups, indicating that the colon-specific germination of CBS and colon-specific enzyme-responsive degradation could improve the intratumoral accumulation of CS@Lipo/Oxp/MTZ significantly.

Moreover, we stained tumor tissues of different groups with H&E staining, TUNEL, Ki67, and ICD markers: CRT and HMGB1 to evaluate pathological changes (Fig. 6F)[49,50]. Compared with PBS, the H&E pathological sections showed the control group presented dense tumor tissues with or without *F. nucleatum*, while the CBS group showed slight necrosis, suggesting that the butyrate produced by probiotics possesses an antitumor effect. The CS@Lipo/Oxp group showed apoptosis and necrosis in portions of tumor tissues, and the addition of MTZ significantly improved the antitumor effect of Oxp. Furtherly, the combination of CBS induced a large necrotic area of the CBS-CS@Lipo/Oxp/MTZ group, with a significant decrease in proliferative cells (Ki67 marker) and a significant increase in apoptotic cells (TUNEL marker). The ICD markers CRT and HMGB1 were also significantly increased. The liver is the favored distant metastatic site of CRC[51]. Liver metastasis is one of the main causes of CRC-related death. Spontaneous formation in the orthotopic colorectal tumor-bearing mice was confirmed in this work, and the metastasis rate in the CBS-CS@Lipo/Oxp/MTZ group was significantly reduced, and the survival time was prolonged (Fig. 6G and H). All the above results collectively demonstrated that CBS-CS@Lipo/Oxp/MTZ has a significant comprehensive antitumor effect. To further investigate the biological safety of the drug delivery system, we conducted pathological tests on the hematological parameters and

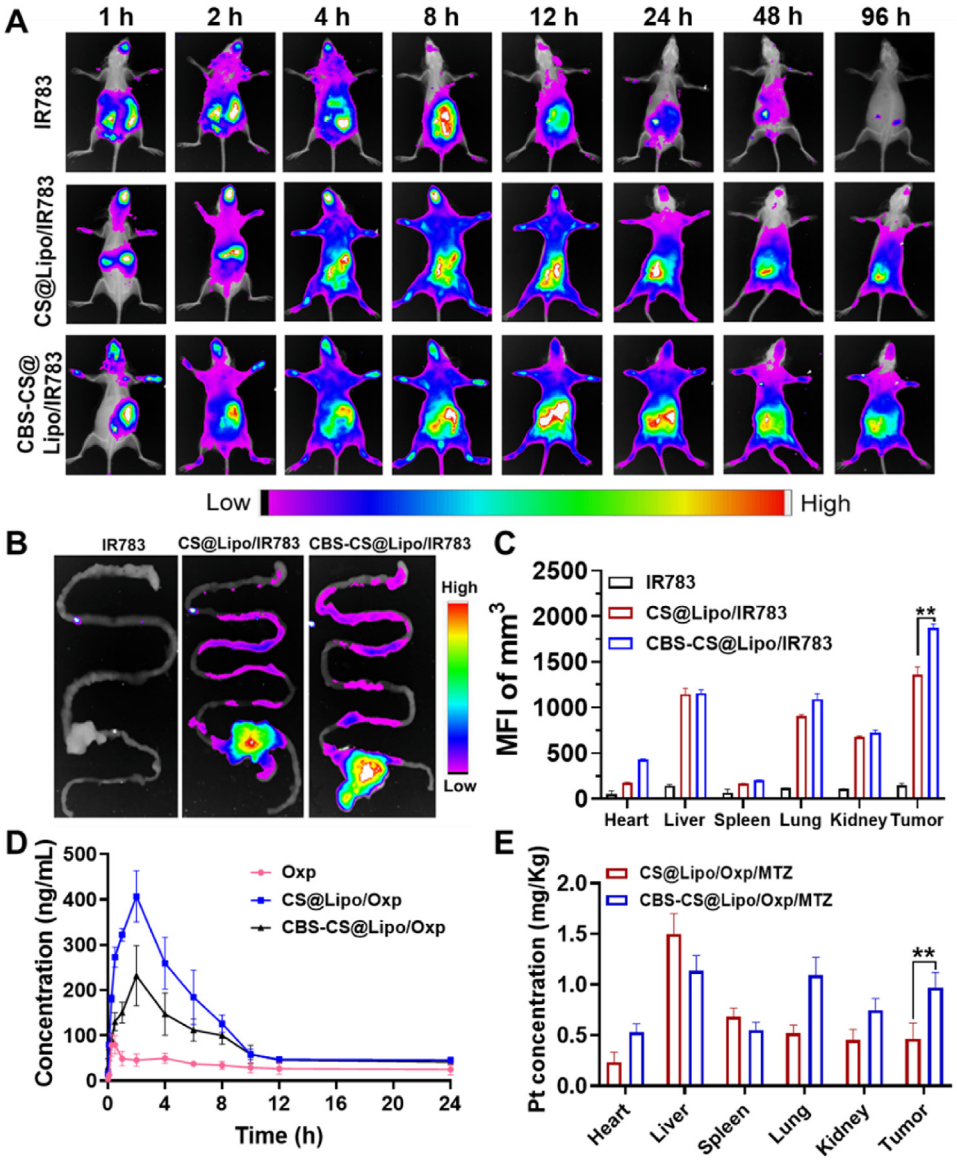

Figure 5 The drug distribution *in vivo*. (A) *In vivo* imaging of CT26 tumor-bearing mice at the indicated time points after oral administration of IR783-labeled formulations: Free IR783, CS@Lipo/IR783, and CBS-CS@Lipo/IR783. (B) The fluorescence images of IR783 distribution in tumors of three groups. (C) The quantified MFI of different tissues. (D) The venous plasma concentration−time profiles of Oxp after oral administration of Oxp, CS@Lipo/Oxp/MTZ, or CBS-CS@Lipo/Oxp/MTZ (10 mg/kg). (E) Quantified distribution in main organs and tumor tissues postinjection by measuring the Pt amount using ICP-MS, data are mean ± SD ($n = 3$), $^{**}P < 0.01$. Each value represents the mean ± SD ($n = 3$ for each group). Statistical analysis by one-way analysis of variance (ANOVA): $^{*}P < 0.05$; $^{**}P < 0.01$; $^{***}P < 0.001$.

main organs of mice. As shown in Fig. S6, there was no significant difference in biochemical indicators between all the experimental groups, indicating that CBS-CS@Lipo/Oxp/MTZ could significantly reduce the toxic side effects of chemotherapy drugs.

3.7. Antitumor immune activation in vivo

To further investigate the antitumor immune response of CBS-CS@Lipo/Oxp/MTZ (+), the immune status of TME was studied by flow cytometry. As displayed in Fig. 7A−C, compared with the PBS (−) group, the increase of MDSCs ($CD45^{+}CD11b^{+}Gr\text{-}1^{+}$), Tregs ($CD45^{+}CD3^{+}CD4^{+}Foxp3^{+}$) and M2-TAMs ($F4/80^{+}CD11b^{+}CD206^{+}$) were observed after treatment with *F. nucleatum*, especially in PBS (+) and CS@Lipo (+), which is consistent with the literature that *F. nucleatum* can recruit immunosuppressive cells to infiltrate tumor tissue, exacerbating the immunosuppressive microenvironment[17,18,52]. The tumor-associated antigens induced by Oxp, along with LPS released by

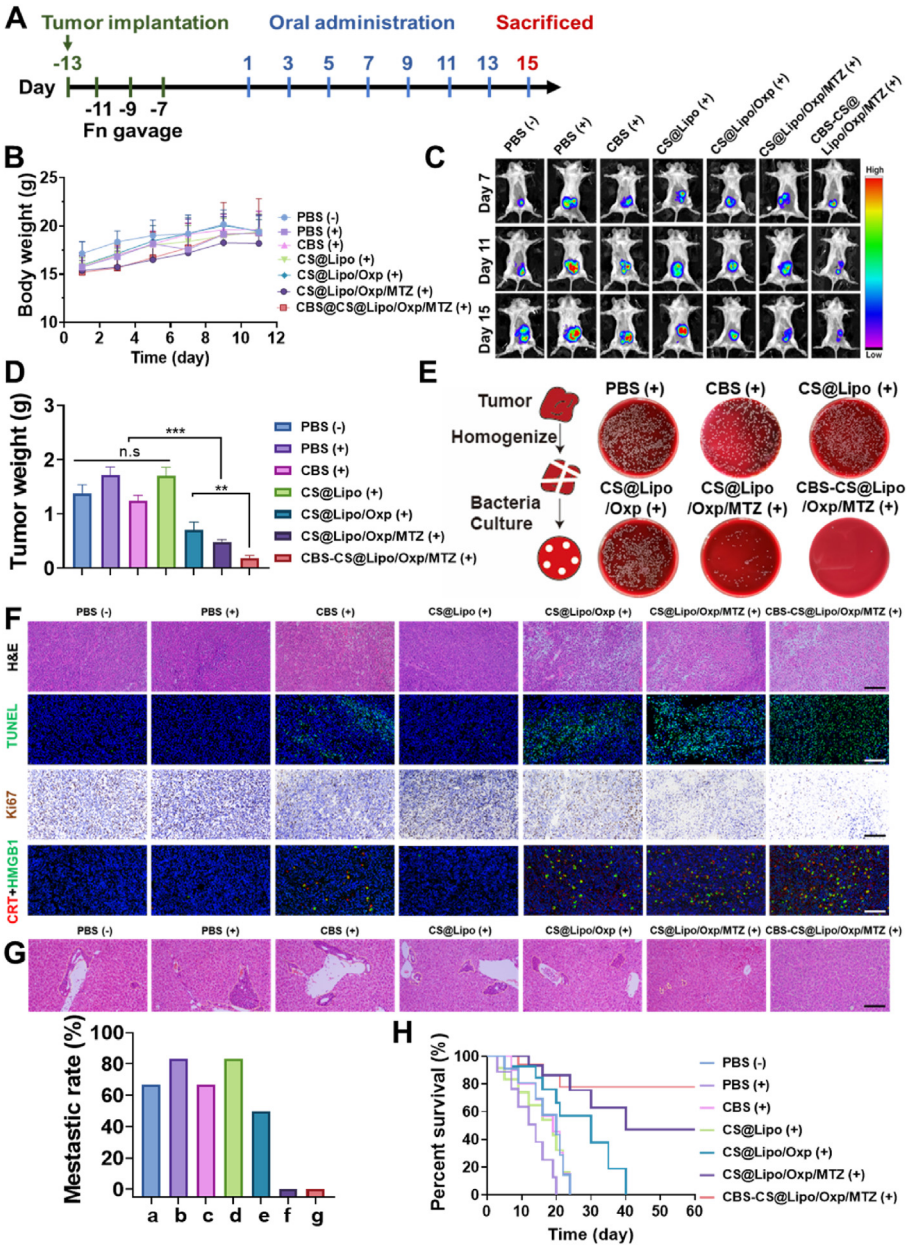

Figure 6 *In vivo* combination therapy in CT26 tumor-bearing mice. (A) Treatment timeline of mice with orthotopic colorectal tumors. (B) The body weight curves of mice after oral administration of different therapeutic formulations. (C) *In vivo* bioluminescence imaging of the mice after receiving PBS (−), PBS (+), CS@Lipo (+), CBS (+), CS@Lipo/Oxp (+), CS@Lipo/Oxp/MTZ (+), CBS- CS@Lipo/Oxp/MTZ (+) (wherein (+) and (−) were referred to incubation in absence or presence of *F. nucleatum*), respectively ($n = 3$). (D) Tumor weight of CRC tissues with two-week treatment. (E) The spread plate of *F. nucleatum* in tumors under the treatment of a: PBS (+), b: CS@Lipo (+), c: CBS (+), d: CS@Lipo/Oxp (+), e: CS@Lipo/Oxp/MTZ (+), f: CBS- CS@Lipo/Oxp/MTZ (+). (F) H&E, TUNEL, Ki67, and CRT + HMGB1 staining, scale bar: 200 μm. (G) H&E analysis of livers and liver metastatic rate. Scale bar: 200 μm. (H) The survival curves of mice with different treatments. Data represent means ± SD ($n = 6$), statistical analysis by one-way analysis of variance (ANOVA): $^{*}P < 0.05$; $^{**}P < 0.01$; $^{***}P < 0.001$.

dead *F. nucleatum*, jointly promote the polarization of TAM towards M1-like phenotype macrophages and the maturation of DCs[53]. Obviously in CS@Lipo/Oxp/MTZ (+) and CBS-CS@Lipo/Oxp/MTZ (+) groups, the ratio of M1-like phenotype macrophages ($CD45^+CD11b^+F4/80^+CD86^+$) were remarkably increased to around 14.1% and 30.0%, and mature DCs ($CD45^+CD11c^+CD80^+CD86^+$) to 35.6% and 52.5%, respectively (Fig. 7D and E). Consistently, the intratumor infiltration of effector T cells ($CD45^+CD3^+CD8^+$) in the CBS-CS@Lipo/Oxp/MTZ (+) group significantly increased from 3.39% to 10.4% compared with CS@Lipo/Oxp (+) group and the $CD4^+$ T cells increased from 14.0% to 28.2%, demonstrating the enhanced immune response of CBS-CS@Lipo/Oxp/MTZ (+) (Fig. 7F). Furtherly, the results of immunofluorescence assay showed the same trend as the flow cytometry (Supporting Information Fig. S7). Secretion of cytokines IFN- *γs* and TNF-*α* also confirmed the effective tumor-specific immune response induced by CBS-CS@Lipo/Oxp/MTZ (+) treatment (Fig. 7G).

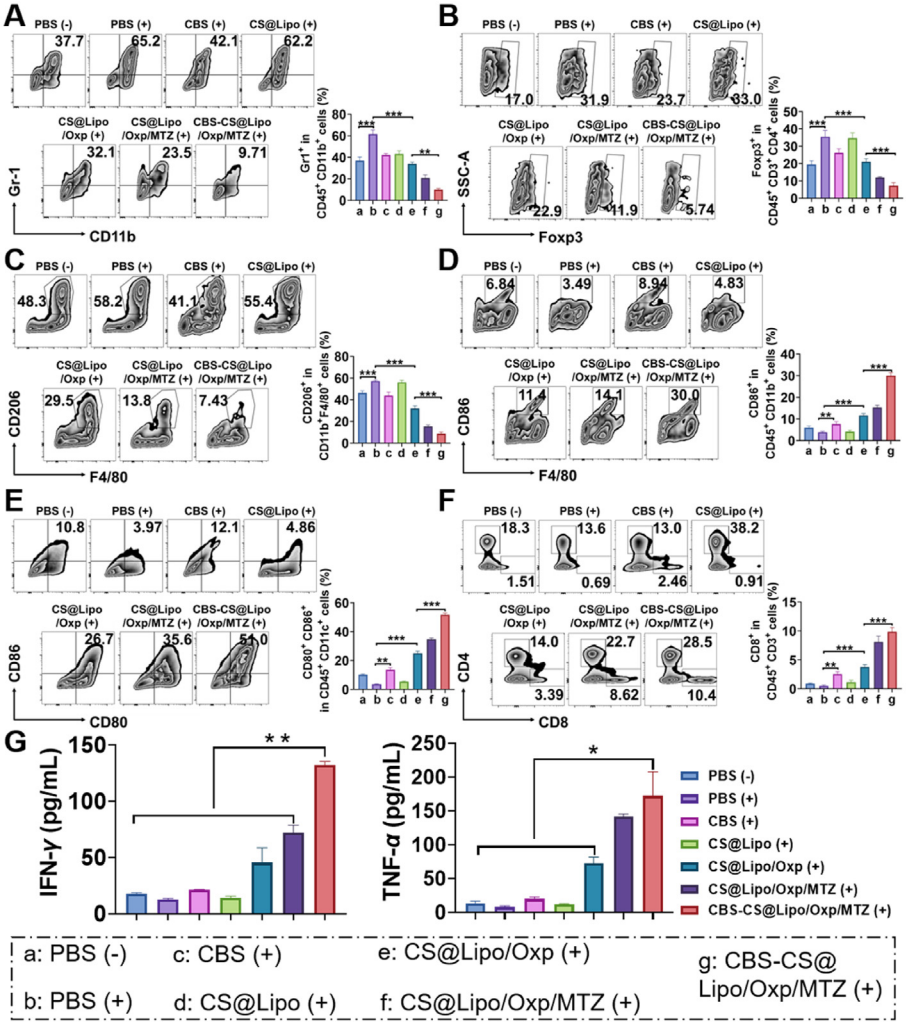

Figure 7 Antitumor immune responses induced by CBS-CS@Lipo/Oxp/MTZ *in vivo*. Representative flow cytometry profiles of (A) MDSCs ($CD11b^+Gr\text{-}1^+$ cells), (B) Tregs ($CD4^+Foxp3^+$ cells), (C) M2-TAMs ($CD11b^+F4/80^+CD206^+$ cells), (D) M1-TAMs ($CD11b^+F4/80^+CD86^+$ cells), (E) Matured DCs ($CD45^+CD11c^+CD80^+CD86^+$ cells), and (F) $CD8^+$ T cells ($CD45^+CD3^+CD8^+$ cells). (G) The Cytokines levels TNF-α and IFN-γ in plasma. Data represent means ± SD ($n = 3$), statistical analysis by one-way analysis of variance (ANOVA): $^*P < 0.05$; $^{**}P < 0.01$; $^{***}P < 0.001$.

Together, CBS-CS@Lipo/Oxp/MTZ (+) demonstrated a powerful ability to reshape ITME.

3.8. *Modulation of CBS-CS@Lipo/Oxp/MTZ on gut microbiota*

The crosstalk between the intestinal pathological microenvironment and TME promotes the tumorigenesis, development, and metastasis of CRC[27,54]. To investigate whether the CBS-CS@Lipo/Oxp/MTZ could improve the therapeutic effect by modulating the composition of intestinal microbiota, 16S rDNA sequencing technology was conducted after two weeks of treatment. According to the alpha diversity analysis (Fig. 8A), the microbiota community richness (Ace) in the PBS (+) group was significantly lower than that in the CBS (+) mice, indicating that probiotics could compete with pathogenic bacteria for colonization and regulate gut microbiota[19]. Conceivably, there was a certain decrease in community richness after CS@Lipo/Oxp/MTZ treatment, suggesting that drug leaking before the target location inevitably has some negative impact on the gut microbiota. Interestingly, the addition of CBS, which is not sensitive to MTZ, can perfectly compensate for the impact of antibiotics[55]. Consistently, the microbiota community diversity (Shannon and Simpson) was also significantly improved after the treatment of CBS-CS@Lipo/Oxp/MTZ. Besides, we analyzed the community abundance of beta diversity at the genus level (Fig. 8B). The dominant bacteria were *Bacteroides, Lactobacillus, Escherichia-Shigella,* and *Akkermansia*. Among them, the abundance of *Lactobacillus* and *Akkermansia* with antitumor effects significantly increased after two weeks of treatment of CBS-CS@Lipo/Oxp/MTZ. Venn chart can be used to count the number of common and unique species in multiple groups. As shown in Fig. 8C, compared to PBS (+), the final formulation group has the highest number of species (349 *VS.* 720). The circos diagram reflected the distribution proportion of dominant species (*Lactobacillus* and *Akkermansia*) of the CBS-CS@Lipo/Oxp/MTZ group were ∼25% and ∼31%, respectively (Supporting Information Fig. S8). Furthermore, cladogram maps were employed to show the significant abundance differences between groups (Fig. 8D).

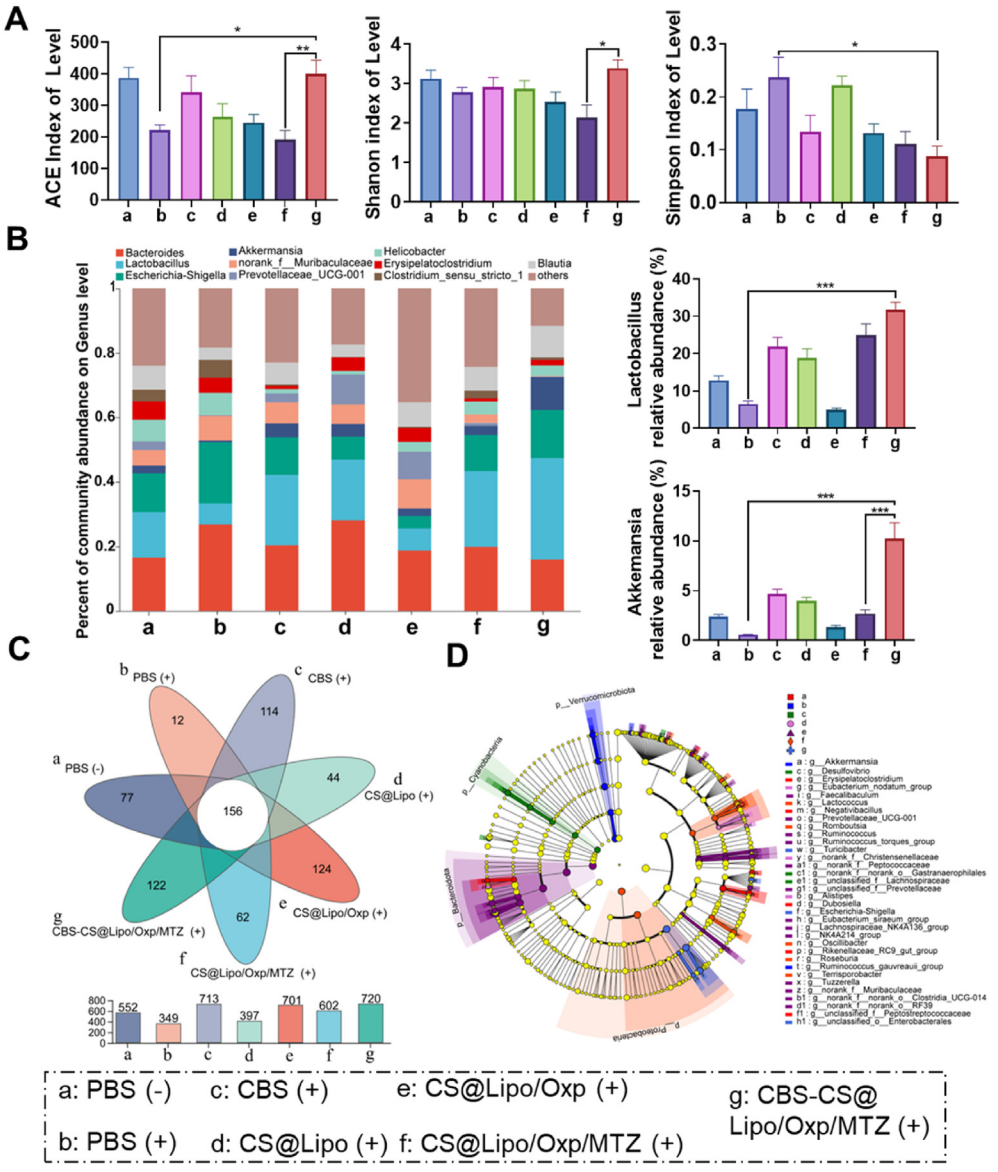

Figure 8 The regulation of CBS-CS@Lipo/Oxp/MTZ in the composition and abundance of gut microbiota. (A) alpha diversity was displayed by ACE, Chao, and Sipmson. (B) Community abundance on the genius level and relative abundance quantification of *Lactobacillus* and *Akkemansia*. (C) Venn chart to count the number of common and unique species in multiple groups. (D) LEfSe taxonomic cladogram detecting significant abundance differences of different treatment groups. Each value represents the mean ± SD ($n = 5$ for each group). Statistical analysis by one-way analysis of variance (ANOVA) and non-parametric factorial Kruskal−Wallis (KW) sum-rank test: $^{*}P < 0.05$; $^{**}P < 0.01$; $^{***}P < 0.001$.

Compared with PBS (+), there were more beneficial bacteria in the CBS-CS@Lipo/Oxp/MTZ group, such as *Lactobacillaceae*, *Akkermansia* and *Blautia*, which were associated with antitumor. Taken together, after two weeks treatment with this microbial agent, there was a significant increase in species abundance of tumor-bearing mice.

4. Conclusions

In summary, we developed an oral colon-targeting drug delivery system (CBS-CS@Lipo/Oxp/MTZ) based on probiotic spores to synchronize colon-specific delivery, intratumoral pathogenic bacteria-killing, and antitumor immunotherapy. On the one hand, by leveraging the colon-specific germination of CBS and colon-specific enzyme-responsive degradation of CS, the colon-specific release of liposomes was achieved, and the intratumoral accumulation of liposomes was enhanced. On the other hand, the localized killing of intratumoral bacteria with antibiotic agent MTZ combined with blocking their supplementation pathway by regulating gut microbiota achieved the fundamental killing of intratumoral pathogenic bacteria. Furtherly, collaborating with SCFAs produced by CB, LPS released from MTZ-induced dead *F. nucleatum* and tumor-associated antigens released by Oxp-caused immunogenic

dead cells jointly promoted the tumor infiltration of $CD8^+$ T cells, reactivating the robust efficacy of chemo-immunotherapy. In general, the combination of nanotechnology and probiotic therapy provides more theoretical and practical basis for the development of a precise and controllable oral delivery system.

Acknowledgments

This work was supported by the National Natural Science Foundation of China (Nos. 82171333, 82272847, 82202318). Postdoctoral Fellowship Program of CPSF (GZB20230675, China). The Henan Province Fund for Cultivating Advantageous Disciplines (No. 222301420012, China). Central Plains Science and Technology Innovation Leading Talent Project (No. 234200510005, China). Graduate Education Reform Project of Henan Province (2023SJGLX127Y, China).

Author contributions

Mengya Niu: Writing − review & editing, Writing − original draft, Software, Methodology, Investigation, Data curation, Conceptualization. Yihan Pei: Validation, Methodology, Data curation. Tiantian Jin: Validation, Methodology, Data curation. Junxiu Li: Software, Methodology, Investigation, Data curation. Liming Bai: Validation, Investigation, Data curation. Cuixia Zheng: Writing − review & editing, Conceptualization. Qingling Song: Writing − review & editing, Funding acquisition, Conceptualization. Hongjuan Zhao: Writing − review & editing, Funding acquisition, Conceptualization. Yun Zhang: Writing − review & editing, Funding acquisition, Conceptualization. Lei Wang: Writing − review & editing, Writing − original draft, Funding acquisition, Conceptualization.

Conflicts of interest

The authors have no conflicts of interest to declare.

Appendix A. Supporting information

Supporting information to this article can be found online at https://doi.org/10.1016/j.apsb.2024.09.015.

References

1. Haddadzadegan S, Dorkoosh F, Bernkop-Schnürch A. Oral delivery of therapeutic peptides and proteins: technology landscape of lipid-based nanocarriers. *Adv Drug Deliver Rev* 2022;**182**:114097.
2. Bhaskaran NA, Kumar L. Treating colon cancers with a non-conventional yet strategic approach: an overview of various nanoparticulate systems. *J Control Release* 2021;**336**:16−39.
3. He HS, Lu Y, Qi JP, Zhu QG, Chen ZJ, Wu W. Adapting liposomes for oral drug delivery. *Acta Pharm Sin B* 2019;**9**:36−48.
4. Lai WF, Wong WT, Rogach AL. Molecular design of layer-by-layer functionalized liposomes for oral drug delivery. *Acs Appl Mater Inter* 2020;**12**:43341−51.
5. Hou Y, Jin JZ, Duan HX, Liu C, Chen LQ, Huang W, et al. Targeted therapeutic effects of oral inulin-modified double-layered nanoparticles containing chemotherapeutics on orthotopic colon cancer. *Biomaterials* 2022;**283**:121440.
6. Hayashi A, Sato T, Kamada N, Mikami Y, Matsuoka K, Hisamatsu T, et al. A single strain of clostridium butyricum induces intestinal IL-10-producing macrophages to suppress acute experimental colitis in mice. *Cell Host Microbe* 2013;**13**:711−22.
7. Liu HR, Xu X, Liang J, Wang J, Li Y. The relationship between clostridium butyricum and colorectal cancer. *J Cancer Res Ther* 2022;**18**:1855−9.
8. Shi LL, Liu XX, Li YZ, Li S, Wu WB, Gao XH, et al. Living bacteria-based immuno-photodynamic therapy: metabolic labeling of clostridium butyricum for eradicating malignant melanoma. *Adv Sci* 2022;**9**:e2105807.
9. Song WF, Yao WQ, Chen QW, Zheng DW, Han ZY, Zhang XZ. *In situ* bioorthogonal conjugation of delivered bacteria with gut inhabitants for enhancing probiotics colonization. *Acs Cent Sci* 2022;**8**:1306−17.
10. He Y, Fu L, Li Y, Wang W, Gong M, Zhang J, et al. Gut microbial metabolites facilitate anticancer therapy efficacy by modulating cytotoxic $CD8^+$ T cell immunity. *Cell Metab* 2021;**33**:988−1000.e7.
11. Xu H, Luo H, Zhang J, Li K, Lee MH. Therapeutic potential of clostridium butyricum anticancer effects in colorectal cancer. *Gut Microbes* 2023;**15**:2186114.
12. Daher E, Rosenberg E, Demain AL. Germination-initiated spores of bacillus-brevis nagano retain their resistance properties. *J Bacteriol* 1985;**161**:47−50.
13. McKenney PT, Driks A, Eichenberger P. The *Bacillus subtilis* endospore: assembly and functions of the multilayered coat. *Nat Rev Microbiol* 2013;**11**:33−44.
14. Freitas C, Plannic J, Isticato R, Pelosi A, Zilhao R, Serrano M, et al. A protein phosphorylation module patterns the *Bacillus subtilis* spore outer coat. *Mol Microbiol* 2020;**114**:934−51.
15. Zhang YG, Zhang JL, Xia YL, Sun J. Bacterial translocation and barrier dysfunction enhance colonic tumorigenesis. *Neoplasia* 2023;**35**:100847.
16. Yu TC, Guo FF, Yu YN, Sun TT, Ma D, Han JX, et al. Promotes chemoresistance to colorectal cancer by modulating autophagy. *Cell* 2017;**170**:548−63.
17. Brennan CA, Garrett WS. Fusobacterium nucleatum—symbiont, opportunist and oncobacterium. *Nat Rev Microbiol* 2019;**17**:156−66.
18. Gur C, Ibrahim Y, Isaacson B, Yamin R, Abed J, Gamliel M, et al. Binding of the fap2 protein of fusobacterium nucleatum to human inhibitory receptor TIGIT protects tumors from immune cell attack. *Immunity* 2015;**42**:344−55.
19. Gopalakrishnan V, Helmink BA, Spencer CN, Reuben A, Wargo JA. The influence of the gut microbiome on cancer, immunity, and cancer immunotherapy. *Cancer Cell* 2018;**33**:570−80.
20. Borowsky J, Haruki K, Lau MC, Costa AD, Vayrynen JP, Ugai T, et al. Association of fusobacterium nucleatum with specific T-cell subsets in the colorectal carcinoma microenvironment. *Clin Cancer Res* 2021;**27**:2816−26.
21. Xu JQ, Xu JC, Shi TF, Zhang YL, Chen FM, Yang C, et al. Probiotic-inspired nanomedicine restores intestinal homeostasis in colitis by regulating redox balance, immune responses, and the gut microbiome. *Adv Mater* 2023;**35**:e2207890.
22. Chen M, Han Q, Zhang M, Liu Y, Wang L, Yang F, et al. Upconversion dual-photosensitizer-expressing bacteria for near-infrared monochromatically excitable synergistic phototherapy. *Sci Adv* 2024;**10**:eadk9485.
23. Li J, Xia Q, Guo H, Fu Z, Liu Y, Lin S, et al. Decorating bacteria with triple immune nanoactivators generates tumor-resident living immunotherapeutics. *Angew Chem Int Ed Engl* 2022;**61**:e202202409.
24. Luo HL, Wu F, Wang XY, Lin SS, Zhang MM, Cao ZP, et al. Encoding bacterial colonization and therapeutic modality by wrapping with an adhesive drug-loadable nanocoating. *Mater Today* 2023;**62**:98−110.
25. Chen ZX, Li JL, Pan P, Bao P, Zeng X, Zhang XZ. Combination gut microbiota modulation and chemotherapy for orthotopic colorectal cancer therapy. *Nano Today* 2021;**41**:e2004529.
26. Geng SZ, Guo PK, Li XL, Shi YR, Wang J, Cao MN, et al. Biomimetic nanovehicle-enabled targeted depletion of intratumoral synergizes with PD-L1 blockade against breast cancer. *Acs Nano* 2024:8971−87.
27. Jiang H, Guo Y, Yu Z, Hu P, Shi J. Nanocatalytic bacteria disintegration reverses immunosuppression of colorectal cancer. *Natl Sci Rev* 2022;**9**:nwac169.
28. Liu XM, Sun MY, Pu F, Ren JS, Qu XG. Transforming intratumor bacteria into immunopotentiators to reverse cold tumors for enhanced

immuno-chemodynamic therapy of triple-negative breast cancer. *J Am Chem Soc* 2023;**145**:26296−307.
29. Gu ZL, Hao Y, Schomann T, Ossendorp F, ten Dijke P, Cruz LJ. Enhancing anti-tumor immunity through liposomal oxaliplatin and localized immunotherapy STING activation. *J Control Release* 2023;**357**:531−44.
30. Li Y, Zhai Y, Liu W, Zhang K, Liu J, Shi J, et al. Ultrasmall nanostructured drug based pH-sensitive liposome for effective treatment of drug-resistant tumor. *J Nanobiotechnology* 2019;**17**:117−30.
31. Yao YK, Chen SY, Cao MT, Fan X, Yang T, Huang Y, et al. Antigen-specific CD8(+) T cell feedback activates NLRP3 inflammasome in antigen-presenting cells through perforin. *Nat Commun* 2017;**8**:15402.
32. Zhang Y, Zhang L, Zheng S, Li M, Xu C, Jia D, et al. Fusobacterium nucleatum promotes colorectal cancer cells adhesion to endothelial cells and facilitates extravasation and metastasis by inducing ALPK1/NF-κB/ICAM1 axis. *Gut Microbes* 2022;**14**:2038852.
33. Song Q, Jia J, Niu X, Zheng C, Zhao H, Sun L, et al. An oral drug delivery system with programmed drug release and imaging properties for orthotopic colon cancer therapy. *Nanoscale* 2019;**11**:15958−70.
34. Setlow P. Spore resistance properties. *Microbiol Spectr* 2014;**2**:1−14.
35. Setlow P, Wang S, Li YQ. Germination of spores of the orders bacillales and clostridiales. *Annu Rev Microbiol* 2017;**71**:459−77.
36. Fu A, Yao B, Dong T, Chen Y, Yao J, Liu Y, et al. Tumor-resident intracellular microbiota promotes metastatic colonization in breast cancer. *Cell* 2022;**185**:1356−72.e26.
37. Nejman D, Livyatan I, Fuks G, Gavert N, Zwang Y, Geller LT, et al. The human tumor microbiome is composed of tumor type-specific intracellular bacteria. *Science* 2020;**368**:973−80.
38. Geller LT, Barzily-Rokni M, Danino T, Jonas OH, Shental N, Nejman D, et al. Potential role of intratumor bacteria in mediating tumor resistance to the chemotherapeutic drug gemcitabine. *Science* 2017;**357**:1156−60.
39. Palucka K, Banchereau J. Cancer immunotherapy *via* dendritic cells. *Nat Rev Cancer* 2012;**12**:265−77.
40. Zanganeh S, Hutter G, Spitler R, Lenkov O, Mahmoudi M, Shaw A, et al. Iron oxide nanoparticles inhibit tumour growth by inducing pro-inflammatory macrophage polarization in tumour tissues. *Nat Nanotechnol* 2016;**11**:986−94.
41. Honda K, Littman DR. The microbiota in adaptive immune homeostasis and disease. *Nature* 2016;**535**:75−84.
42. Yang R, Wei T, Goldberg H, Wang WP, Cullion K, Kohane DS. Getting drugs across biological barriers. *Adv Mater* 2017;**29**:1606596.
43. Brunner J, Ragupathy S, Borchard G. Target specific tight junction modulators. *Adv Drug Deliver Rev* 2021;**171**:266−88.
44. Cox KE, Liu SL, Hoffman RM, Batra SK, Dhawan P, Bouvet M. The expression of the claudin family of proteins in colorectal cancer. *Biomolecules* 2024;**14**:272−96.
45. Nehme Z, Roehlen N, Dhawan P, Baumert TF. Tight junction protein signaling and cancer biology. *Cells-Basel* 2023;**12**:243−65.
46. Sougiannis AT, VanderVeen BN, Enos RT, Velazquez KT, Bader JE, Carson M, et al. Impact of 5 fluorouracil chemotherapy on gut inflammation, functional parameters, and gut microbiota. *Brain Behav Immun* 2019;**80**:44−55.
47. Wang J, Li J, Yu J, Zhang H, Zhang B. Large hollow cavity luminous nanoparticles with near-infrared persistent luminescence and tunable sizes for tumor afterglow imaging and chemo-/photodynamic therapies. *ACS Nano* 2018;**12**:4246−58.
48. Jiang SS, Xie YL, Xiao XY, Kang ZR, Lin XL, Zhang L, et al. Fusobacterium nucleatum-derived succinic acid induces tumor resistance to immunotherapy in colorectal cancer. *Cell Host Microbe* 2023;**31**:781−97.e9.
49. Obeid M, Tesniere A, Ghiringhelli F, Fimia GM, Apetoh L, Perfettini JL, et al. Calreticulin exposure dictates the immunogenicity of cancer cell death. *Nat Med* 2007;**13**:54−61.
50. Deng H, Yang W, Zhou Z, Tian R, Lin L, Ma Y, et al. Targeted scavenging of extracellular ROS relieves suppressive immunogenic cell death. *Nat Commun* 2020;**11**:4951.
51. Gao Y, Bado I, Wang H, Zhang W, Rosen JM, Zhang XH. Metastasis organotropism: redefining the congenial soil. *Dev Cell* 2019;**49**:375−91.
52. Janney A, Powrie F, Mann EH. Host-microbiota maladaptation in colorectal cancer. *Nature* 2020;**585**:509−17.
53. He TT, Wang L, Gou SQ, Lu L, Liu GH, Wang K, et al. Enhanced immunogenic cell death and antigen presentation *via* engineered bifidobacterium bifidum to boost chemo-immunotherapy. *Acs Nano* 2023;**17**:9953−71.
54. Wong SH, Yu J. Gut microbiota in colorectal cancer: mechanisms of action and clinical applications. *Nat Rev Gastroenterol Hepatol* 2019;**16**:690−704.
55. Liu X, Qiu XY, Yang Y, Wang J, Wang Q, Liu JB, et al. Alteration of gut microbiome and metabolome by clostridium butyricum can repair the intestinal dysbiosis caused antibiotics in mice. *Iscience* 2023;**26**:106190.